Multi-objective Optimization of a Tubular Coreless LPMSM Based on Adaptive Multi-objective Black Hole Algorithm

Tao Wu, *Member, IEEE,* Zhenan Feng, Chong Wu, Gang Lei, *Member, IEEE,* Youguang Guo, *Senior Member, IEEE,* Jianguo Zhu, *Senior Member, IEEE,* and Xinmei Wang

Abstract—In most multi-objective optimization problems of electrical machines, the weighted function method is used to convert them into single-objective optimization problems. This paper applies a kind of new multi-objective evolutionary algorithms (MOEAs), called adaptive multi-objective black hole (AMOBH) algorithms, to achieve effective multi-objective optimization of a tubular coreless linear permanent magnet synchronous motor (LPMSM). To reduce the computation cost of the MOEAs, a one-layer analytical model (AM) is presented for the tubular coreless LPMSM in this paper. The accuracy of the simplified one-layer AM is verified by comparisons with multi-layer AM and finite element analysis (FEA) under different structure parameters. It is found that the simplified AM has good accuracy and can decrease the computation cost significantly. AMOBH algorithm is subsequently introduced. The optimal Pareto front with regard to thrust, copper loss and permanent magnet volume are analyzed, and more diversified optimization results are provided. The final Pareto solution can be selected directly by practical physical values according to the application requirements. Finally, a prototype is fabricated for the selected design; its experimental results are provided and compared with those of the FEA results.

Index Terms—Multi-objective optimization, analytical method, linear permanent magnet synchronous motor.

Manuscript received Nov, 2018; revised Feb, 2019; second revised Mar 2019, accepted Apr, 2019. The work was supported by the Natural Science Foundation of China under Grant (No.61603358 and No.61703376), and the Open Research Fund of Research Center for Advanced Control of Complex Systems and Intelligent Geoscience Instrument, China University of Geosciences (Wuhan) (No. AU2015CJ018).

Tao Wu, Zhenan Feng and Xinmei Wang are with the School of Automation, China University of Geosciences, Wuhan, 430074, China, and the Hubei Key Laboratory of Advanced Control and Intelligent Automation for Complex Systems (e-mails: wutao@cug.edu.cn, fengzhenan@cug.edu.cn, wangxm@cug.edu.cn).

Chong Wu is with the Department of Electronic Engineering, City University of Hong Kong, Kowloon, Hong Kong (e-mail: chongwu2-c@my.cityu.edu.hk).

Jianguo Zhu is with the School of Electrical and Information Engineering, University of Sydney, Sydney NSW 2006, Australia (e-mail: jianguo.zhu@sydney.edu.au).

Gang Lei and Youguang Guo are with the School of Electrical and Data Engineering, University of Technology, Sydney NSW 2007, Australia (e-mails: gang.lei@uts.edu.au, youguang.guo-1@uts.edu.au).

Corresponding author: Gang Lei. (phone: +61-2-95141268, fax: +61-2-95141810, e-mail: gang.lei@uts.edu.au)

I. INTRODUCTION

Recently, the linear permanent magnet (PM) synchronous motor (LPMSM) has gained more and more applications in industry and other areas, especially in high speed and high precision servo applications [1], [2], and linear oscillatory actuator (LOA) system (refrigerators/compressors) [3–5]. The LPMSM avoids rotary-to-linear conversion mechanism and generates linear motion directly, which contributes to structure simplification and improvement of work efficiency. Due to the manufacturing complexity of the tubular

laminated core, the tubular coreless LPMSM (without slots) is an economic and commonly used type, which has advantages of zero detent force, light weight and high acceleration performance [6], [7]. It also has no lateral edge effect that exists in the flat one and it is very suitable for some cylindrical applications such as linear compressors, electric power switch plunger solenoids [4], and electromagnetic hammer [8], [9].

To improve the performances of LPMSM under different conditions, the multi-objective optimization has been applied to motor design in previous researches [10]. The commonly used calculation models of the electrical machines include the finite-element model (FEM) [11], [12] and the analytical model (AM) [13], [14]. As to the major electrical machines, it is hard to establish an accurate AM for optimization algorithm because of their complex structure and the nonlinear magnetic circuit. Therefore, the optimization methods coupled with FEM become prevalent and practical, especially in high dimensional problems [11], [12], [15]. At the same time, as to the coreless LPMSM there is no iron core and slots among the coils, so its magnetic circuits are nearly linear. The AMs for the magnetic field, thrust and back-EMF have been deduced and analyzed in many previous works. Refs. [13] and [14] introduced a multi-objective optimization of air-core LPMSM (flat) based on a multilayer model. The AM (magnetic field distribution, EMF, and thrust force) of a tubular modular PM machine equipped with quasi-Halbach magnetized magnets has been deduced in [16] and [17]. The magnetic field is worked out by solving differential equations according to the boundary conditions at different regions. For example, there are three regions in a non-magnetic tubular coreless LPMSM. The coefficients of the differential equation solution are calculated very tediously and time-consumingly. In linear motor optimization, the properties and characteristics of the motor obtained by single-objective optimization can provide some empirical help for multistage optimization, such as offering the selection of weights in the thermal calculation, iron losses calculation and magnet losses calculation of the motor, so that it can derive theoretical basis of its calculation through the corresponding model [18–20].

Usually, the optimization objectives in electrical machines include the maximization of the average thrust and power density, and minimization of the torque ripple, power loss and material cost. Moreover,

these objectives are often conflicting with each other under the constraints. Nearly all the multi-objective optimization problems (MOPs) in electrical machines use the weight function to transform MOPs into single-objective optimization problems (SOPs) to simplify the solution process [21]. However, to transform MOPs into SOPs requires some prior knowledge to assign weight coefficients and it can only obtain one solution of the Pareto optimal solution set. The decision of weight coefficients will determine the result of optimization to a large extent which may reduce the feasibility of the results [22], [23]. Unlike the SOPs, there are multiple global optimum solutions which are called Pareto optimal solutions in MOPs. Also, these objectives are often conflicting with each other. Commonly used multi-objective evolutionary algorithms (MOEAs) are as follows: multi-objective particle swarm optimization (MOPSO) [24], non-dominated sorting genetic algorithm II (NSGA-II) [25] and multi-objective evolutionary algorithm based on decomposition (MOEA/D) [26], Ref. [27] proposed a

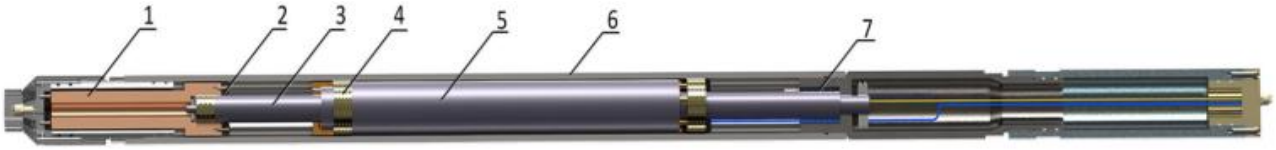

Fig. 1. Structure of the hammer driven by tubular coreless LPMSM.

novel multi-objective optimization algorithm called adaptive multi-objective black hole algorithm (AMOBH), which has a good performance in terms of convergence rate, population diversity, population convergence, and subpopulation obtention of different Pareto regions. Although many new algorithms for multi-objective evolutionary computation have emerged in solving engineering problems recently, they have rarely been applied in electrical machines in previous publications. The overall complexity of MOEAs is approximately $O(MN^2)$ or $O(MN^3)$, where M is the number of objectives, and N is the number of Pareto solutions. For example, if M = 3 and N = 50, the total computations are about 7500.

The primary purpose of this paper is to apply AMOBH algorithm to achieve effective multi-objective optimization of a tubular coreless LPMSM used in drilling project [8]. To simplify and reduce the calculations of MOEAs, we present a one-layer AM of the tubular coreless LPMSM in this paper. The scalar field on the boundary interface is estimated by the average working magnetic intensity H_{pm}. The

accuracy of the simplified one-layer AM is verified by comparisons between AM and finite element analysis (FEA) under different structure parameters. AMOBH algorithm has been developed recently which is based on several entropy controlled adaptive evolutionary strategies, black hole (BH) algorithm [28], and a new individual density evolution metric called cell density. The searching solutions, which belong to the Pareto front regard to thrust, copper loss and PM volume, are analyzed. Finally, the diversity of the solutions is compared and the validity of the analytical results is verified by the FEA and experiments. There are two main contributions of this paper: (1) A new simplified and accurate one-layer AM which can increase the computation efficiency significantly compared with the multi-layer AM and FEA; (2) Successful application of the MOEAs to solve multi-objective optimization design of electrical machines, which provides more diversified and global optimization results.

II. Motor Structure and Analytic Model

A. Motor Structure

Fig. 1 illustrates the actual design structure of the electromagnetic hammer driven by tubular LPMSM. Part 1 is an impact anvil. Parts 2 and 7 are the buffer cushion and the buffer springs. Parts 3 and 5 are the stator (toroidal PM and iron bar) and the mover (coils and iron yoke), respectively. In order to ensure the smooth motion of the mover, a ball bearing, indicated by 4, is used to reduce the friction between the mover and the shell of hammer 6.

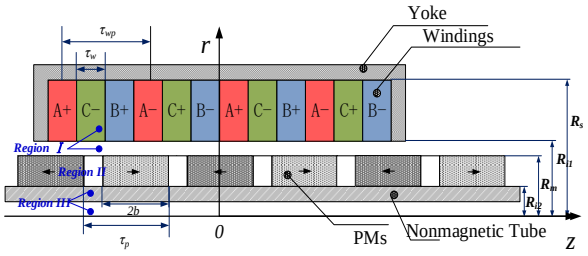

Fig. 2. Structural diagram of the tubular coreless LPMSM.

The structural diagram of the tubular LPMSM is shown in Fig. 2, where b is a half width of the ring PM, τ_p is the pole pitch, τ_{wp} is the coil axial distance which equals τ_p, τ_w is the axial width of one phase coil, R_s is

the outer radius of the coil (Mover), R_{i1} is the inner radius of the coil (Mover), R_{m} is the outer radius of PM (Stator), and R_{i2} is the inner radius of PM (Stator).

B. Analytical Model

According to the material properties, the solution regions in the AM are often divided into different layers as shown in Fig. 2. Regions I and III are the air area, and Region II is the PM area. The general solutions of the differential equation in each region are expressed as

$$\varphi_I(r,z)=\sum_{n=1,3,5}^{\infty}(C_1e^{\lambda r}+C_2e^{-\lambda r})\cos(\lambda z) \qquad (1)$$

$$\varphi_{II}(r,z)=\sum_{n=1,3,5}^{\infty}(C_3e^{\lambda r}+C_4e^{-\lambda r})\cos(\lambda z) \qquad (2)$$

where φ_{I}, φ_{II} are the scalar potentials of Region I and Region II, $\lambda=n\pi/\tau_p$. The coefficients C_1, C_2, C_3 and C_4 are calculated by the boundary conditions which are defined by

$$H_I(r_{\mathrm{m}},z)=H_{II}(r_{\mathrm{m}},z),B_I(r_{\mathrm{m}},z)=B_{II}(r_{\mathrm{m}},z) \quad (3)$$

$$H_{III}(r_{i2},z)=H_{II}(r_{i2},z),B_{III}(r_{i2},z)=B_{II}(r_{i2},z) \quad (4)$$

$$H_I(r_s,z)=0,B_I(r_s,z)=0 \qquad (5)$$

Since the coefficients' expressions deduced in the appendix of [16] are very complicated, a simplified one-layer AM is presented below. What is more，the solution process may be much more complicated if the material between the PM in Region II is magnetic (iron core). The iron core can make the magnetic flux density in Region I within this area much flatter and stronger.

1) Magnetic Field Model

The PMs adopt axial magnetization as shown in Fig. 2. Assuming that the scalar magnetic potential on the interface between Region I and Region II is also considered as a rectangular wave, the Fourier expansion of the rectangular magnetic potential is

$$\varphi_z=\frac{4H_{pm}}{(2n-1)\pi}\sum_{n=1}^{\infty}\sin(mb)\sin(mz)=H_{pm}\sum_{n=1}^{\infty}F_m\sin(mz) \quad (6)$$

where H_{pm} denotes H_I in (3) which has a physical meaning that provides the external magnetic potential for

Region I and its another physical meaning is the magnetic intensity at the working point of the PM, b is half-length of the PM in magnetization direction, $m=(2n-1)\pi/\tau_p$ and $F_m=4\sin(mb)/(m\tau_p)$. Actually, the magnetic intensity of the PM in different cross-sectional areas and at different locations is not the same as shown in Fig. 3. In order to simplify the calculation, it can be assumed that the PM are a homogeneous magnet and the average working magnetic intensity H_{pm} is considered as the operating point of an entire PM [29], [30].

Assume that the PM is uniformly magnetized and the operating point $P\ (B_{pm}, H_{pm})$ is shown as in Fig. 4, where B_{pm} is the average flux density at the working point of the PM, B_{r0} is the residual magnetic flux density of the PM and μ_r is the relative permeability of the PM.

$$H_{pm}=\frac{B_{r0}\text{-}B_{pm}}{\mu_0 u_r} \tag{7}$$

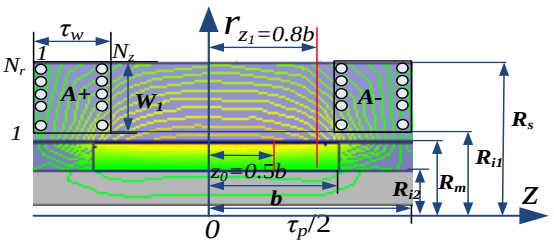

Fig. 3. The calculation model for the back-EMF.

The magnetic field AM of the tubular coreless LPMSM is an axisymmetric model, the scalar magnetic potential has nothing to do with θ, and there is no current in the solution area, so

$$\nabla^2\varphi(r,z)=0 \tag{8}$$

and the boundary conditions in Region I are as follows,

$$r=R_{\mathrm{m}},R(r)=\varphi_m,r=\infty\approx 10R_{\mathrm{s}}=R_{\mathrm{s1}},and\ R(r)=0 \tag{9}$$

Using the method of separation of variables to solve the Laplace differential equation of (8), one obtains,

$$\varphi(r,z)=\frac{\varphi_m}{\Delta_1}\Delta_2(r)\sin(mz) \tag{10}$$

where

$$\Delta_1=I_0(mR_{\mathrm{s1}})K_0(mR_{\mathrm{m}})-I_0(mR_{\mathrm{m}})K_0(mR_{\mathrm{s1}})$$

$$\Delta_2 = I_0(mR_{s1})K_0(mr) - I_0(mr)K_0(mR_{s1}) \quad \Delta_3(r) = I_0(mR_{s1})K_1(mr) + I_1(mr)K_0(mR_{s1})$$

I_0 and K_0 are the first class and the second class of zero order deformation Bessel function, and I_1 and K_1 are the first and second class zero-order modified Bessel functions, respectively.

The radial magnetic flux density can be calculated as $B_r(r,z) = -\mu_0 \dfrac{d\varphi(r,z)}{dr}$

$$B_r(r,z) = \sum_{n=1}^{\infty} \frac{\mu_0 m |H_{pm} F_m|}{\Delta_1} \Delta_3(r) \sin(mz) \qquad (11)$$

2) Electromagnetic Thrust Calculation Model

The formula of Ampere force can be deduced by

$$\mathrm{d}F_z(r,z) = 2\pi B_r(r,z) J_m dr dz \qquad (12)$$

where J_m is the current density of the coil winding. The thrust of tubular coreless LPMSM can be described as the following:

$$\begin{aligned} F = \sqrt{2} J_m \sum_{n=1}^{\infty} K_{Tn} \Big[& \cos\left(m\left(z - \tau_p\right)\right) \sin(\omega t) \\ & + \cos m\left(z - \frac{7\tau_p}{6}\right) \sin\left(\omega t - \frac{2\pi}{3}\right) \\ & + \cos m\left(z + \frac{\tau_p}{6}\right) \sin\left(\omega t + \frac{2\pi}{3}\right) \Big] \end{aligned} \qquad (13)$$

where

$$K_{Tn} = -4\pi p K_{wn} \frac{m\mu_0 H_{pm} b F_m \tau_w}{\Delta_1} \int_{R_{i1}}^{R_s} r \Delta_3(r) dr \quad (14)$$

$K_{wn} = K_1 K_2$ is the (2n-1) -th order's winding coefficient, $K_1 = \sin(m\tau_{wp}/2)$ is the (2n-1) -th order's harmonic winding coefficient, and $K_2 = \sin(m\tau_w/2)/(m\tau_w/2)$ is the (2n-1) -th order's winding distribution coefficient.

3) Back-EMF and Copper Loss Calculation Model

General speaking, the coils are usually composed by the toroidal windings in tubular LPMSM. Assuming that one phase coil (for example A+) has N_z turns in the axial direction z and N_r turns in the radial direction as shown in Fig. 3, the total number of conductors is $N = N_z N_r$. The coils are divided into N_r layers in the

radial direction. The radial flux densities at different radial positions have different values, shown as Figs. 5–9. In Fig. 3, $N_z : N_r = \tau_w : W_1 = \frac{1}{3}\tau_p : W_1$ here $W_1 = R_s - R_{i1}$ is the coils' radial width. For example, coils of Phase A in axial *z*-axis from 1 to N_z can be regarded as N_z distributed windings, the distribution coefficient of the induced voltage is as

$$k_q = \frac{\sin(\pi / 6)}{N_Z \sin(\pi / 6N_Z)} \tag{15}$$

The instantaneous value of phase A's back-EMF is as

$$e_a = 2N_z \sum_{i=1}^{Nr} B_r(r_i, z) 2\pi r_i v_s = 8\pi\tau_p f N_z k_q \sum_{i=1}^{N} B_r(r_i, z) r_i \tag{16}$$

where r_i is the radius of the N_r-*th* coils. The peak value of the radial flux density B_{rm} is calculated by the following

$$B_{rm}(r_i) = B_r(r_i, z)|_{(z=\tau_p/2)} = \sum_{n=1}^{\infty} \left(\frac{\mu_0 | H_{pm} F_m |}{\Delta_1}\right) \Delta_3(r) \tag{17}$$

Therefore, the peak back-EMF value of phase A is as

$$E_m = 8\pi\tau f N_x k_q \sum_{i=1}^{Nr} B_{rm}(r_i) r_i \tag{18}$$

The section area of winding A+ is

$$s_1 = \tau_w W_1 \tag{19}$$

Assuming that the slot full rate coefficient is S_p = 0.85 (Although there are no slots for coils), the cross-sectional area of the enameled wire can be calculated as

$$s_d = s_1 s_p / N \tag{20}$$

The resistance of phase A is calculated as

$$R = \rho N_x \sum_{i=1}^{Nr} 2\pi (R_{i1} + (R_s - R_{i1}) / N_r i) / s_d \tag{21}$$

where ρ is the resistivity of copper.

The copper loss of three phases is

$$P_{cua} = 3(J_m s_d)^2 R \tag{22}$$

where J_m is the current density.

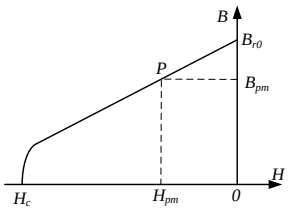

Fig. 4. The demagnetization curve and working point of the permanent magnet.

4) The Work Point of PM under different parameters

The calculation accuracy of H_{pm} has significant influences on the whole AM including thrust, flux density and back-EMF. The magnetic flux lines are shown in Fig. 3. Actually, the magnetic fluxes in any section are not the same, even though in one section the magnetic intensity near the air-gap is larger than that far from the air-gap. Ref. [29] has proposed a method to calculate H_{pm} in which the middle cross-section at $z_0 = 0.5b$ in Fig. 4 is adopted as the calculated section in the slotted tubular LPMSM. However in the coreless one, for the boundary conditions are changed as formula (9) and the magnet gathering effect of the iron core between the PMs, it is found that when the cross-section is chosen at $z_1 = 0.8b$, the magnetic densities at specified radii under different structure parameters are very consistent with each other. The total radial magnetic flux from $z_1 = 0.8b$ to $z = \tau_p / 2$ under a half pole distance at $r = R_m$ is,

$$\Phi_1 = 2\pi R_{\mathrm{m}} \int_{z_1}^{\tau_p/2} B_r\left(R_{\mathrm{m}}, z\right) \sin\left(mz\right) dz \qquad (23)$$

and the total axial magnetic flux in this selected section of the PM ($z_1 = 0.8b$) is as

$$\Phi_2 = B_{pm} S = B_{pm} \pi \left(R_{\mathrm{m}}^2 - R_{i2}^2\right) = \mu_0 \sigma H_{pm} \pi \left(R_{\mathrm{m}}^2 - R_{i2}^2\right) \qquad (24)$$

where σ is a parameter that is only related to the geometry of the motor. According to $\Phi_1 = \Phi_2$, it can be obtained by

$$\sigma = \frac{2R_{\mathrm{m}}}{R_{\mathrm{m}}^2 - R_{i2}^2} \int_{z_1}^{\tau_p/2} \sin(mz) \sum_{n=1}^{\infty} \frac{F_m \Delta_3\left(R_{\mathrm{m}}\right)}{\Delta_1} dz \qquad (25)$$

Figs. 5–9 show the radial flux density at different radii along z-axis by using the AM and FEM. The solid curves are calculated by AM and the dotted curves are calculated by FEM. The lengths (2*b*) of the PMs are

50, 60, 70 and 80 mm, respectively, the thicknesses (W_2 = R_m - R_{i2}) of the PMs are 5 and15 mm, respectively. The solutions are given under the conditions B_{r0} = 1.1 T, μ_r =1.1, R_s = 34 mm. As shown, the results obtained by the AM align well with those by the FEM in the flat area while the FEM waveform increases sharply in the dividing line between the iron core and the PM. The calculation time of one-layer AM (iteration number n = 10,100 points along x axis) is about 2.12 s and that of the multi-layer AM is about 18.23 s (Fig. 5). Although the accuracy of the one-layer AM is slightly lower, it is more suitable for the MOEAs because the computation time can be reduced by 88.03%.

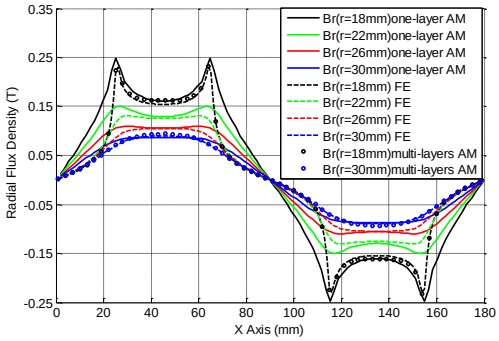

Fig. 5. The radial flux density comparison at different radii by one-layer AM, multi-layer AM and FEM (2b = 50 mm, W_2 = 5 mm, τ_p = 180 mm and R_m = 17 mm)

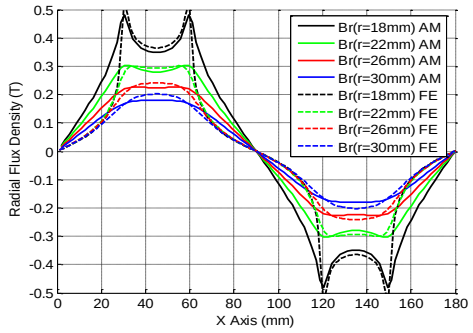

Fig. 6. The radial flux density comparison at different radii by AM and FEM (2b = 60 mm, W_2 = 15 mm, τ_p = 180 mm and R_m = 17 mm)

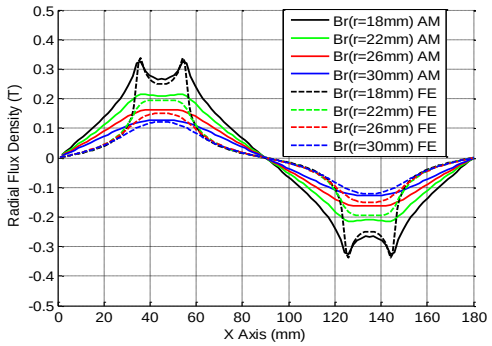

Fig. 7. The radial flux density comparison at different radii by AM and FEM (2b = 70 mm, W_2 = 5 mm, τ_p = 180 mm and R_m = 17 mm)

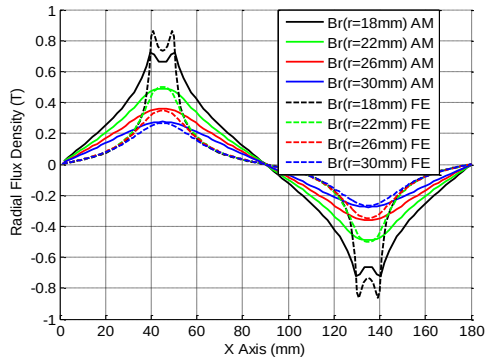

Fig. 8. The radial flux density comparison at different radii by AM and FEM (2b = 80 mm, W_2 = 15 mm, τ_p = 180 mm and R_m = 17 mm)

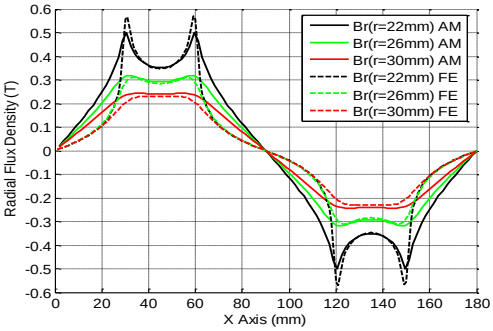

Fig. 9. The radial flux density comparison at different radii by AM and FEM (2b = 60 mm, W_2 = 15 mm, τ_p = 180 mm and R_m = 21 mm)

III. Adaptive Multi-objective Black Hole Algorithm

Population diversity and convergence performance are two important properties of a good multi-objective optimization algorithm. And there is a trade-off between convergence and diversity. Many multi-objective optimization algorithms have a problem of how to achieve a good balance between them.

To solve this problem, a novel multi-objective optimization algorithm called AMOBH has been developed [27]. It is based on the black hole (BH) algorithm. Different from the BH algorithm (original single objective version), AMOBH searches the entire space of solutions (stars) and finds the multiple global optimum solutions (Pareto solutions).

Compared to some state-of-the-art methods, such as NSGA-II [25] and MOEA/D [26], AMOBH outperforms them in terms of convergence performance, population diversity, and computation efficiency. The details of AMOBH can be referred in [27]. The flowchart of AMOBH algorithm is shown as follow.

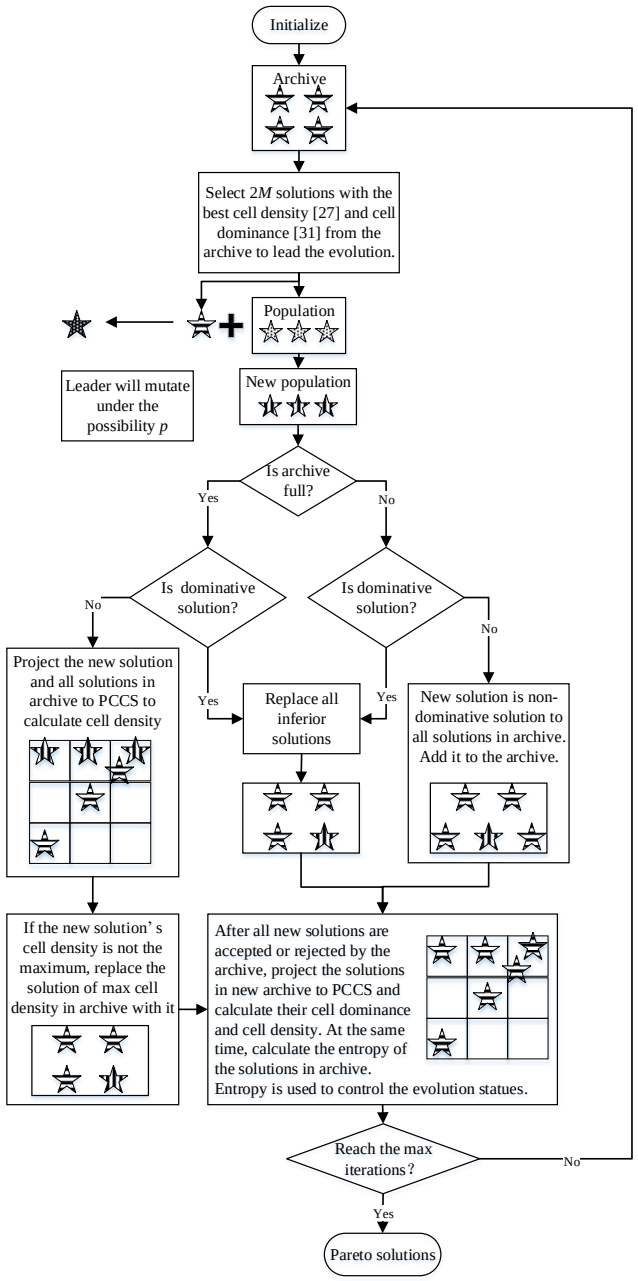

Fig. 10. AMOBH algorithm flowchart

Here, the entropy represents the uniformity and diversity of approximate Pareto solutions. Larger entropy means better uniformity and diversity [31]. AMOBH will first randomly initialize a population set and select several solutions from this set to form the initial archive based on cell density [27] and cell dominance [31]. Then it enters the main loop: (1) Firstly, the algorithm will select several leading solutions from the archive to lead population evolving. To keep good diversity, leaders also will mutate under a certain possibility. (2) Next, the algorithm will determine whether or not to accept the new solution to the archive. (3) Then, after all solutions are accepted or rejected, the algorithm will calculate the entropy of the new archive based on the parallel cell coordinate system (PCCS) [31] and update the evolution status. (4) Finally, the algorithm will output the Pareto solutions, if it reaches the max iterations. If not, it will continue (1)-(4).

IV. Optimization and comparison

To replace the hydraulic or pneumatic hammer in the drilling project, the coreless tubular LPMSM was developed as a new application in petroleum and geological engineering [8]. Due to the special application conditions, the outer diameter of the hammer is limited less than 90 mm (drill pipe's passing diameter). As a result, the diameter of the LPMSM should be designed less than 68 mm. In order to acquire sufficient impact energy as the hydraulic or pneumatic hammer (single impact energy is about 40–80 J), the thrust of the electromagnetic hammer shall be designed as large as possible. What is more, the down hole temperature is quite high and the cooling conditions are relatively poor, so the copper loss of the motor shall be designed as small as possible.

For the optimization task, five design variables are selected as components of the input vector. The chosen design variables are listed in Table I, together with the value ranges. The other design parameters are shown in Table II, in which the air gap and the polar distance are constant.

TABLE I

Optimization Design Variables of the Tubular LPMSM

Variable	Symbol	Unit	Initial Value	Range
Outer radius of coil	R_s	mm	34	$R_{i1}<R_s\leq 34$
Outer radius of PM	R_m	mm	17	$R_{i2}+5< R_m<Rs$
Inner radius of PM	R_{i2}	mm	9	$5< R_{i2}<28$
Width of PM	$2b$	mm	60	$0.5\tau_p<2b<0.9\tau_p$
Number of coils	N	--	350	--

TABLE II

OTHER DESIGN PARAMETERS OF THE TUBULAR LPMSM

PARAMETERS	Symbol	Unit	Value
Air gap	σ_s	mm	1
Polar distance	τ_p	mm	90
Inner radius of coil	R_{i1}	mm	$R_m+\sigma_s$
Current density	J_m	A/mm^2	4
Rated speed	v_N	m/s	9

The input vector x can be described as following:

$$x=[R_s, R_m, R_{i2}, b, N]$$

The optimization objectives of the tubular coreless LPMSM here are chosen to maximize the thrust and the efficiency (copper loss ratio), minimize the PM consumption (the maximum problems are changed to its dual problem). The objective functions are defined as follows,

$$\begin{aligned} \min: \quad & f_1(x)=\frac{C_f}{F}, \\ & f_2(x)=\frac{C_f P_{cua}}{P_{out}+P_{cua}}=\frac{C_f P_{cua}}{F_{vN}+P_{cua}}, \\ & f_3(x)=C_f V_{PM}=C_f 4\pi b(R_m^2-R_{i2}^2), \end{aligned} \tag{26}$$

s.t.

$$200\leq g_1(x)=E_m\leq 380,$$
$$g_2(x)=250-F<0,$$

where F is the thrust by (14), P_{cua} is the copper loss by (23), and E_m is the back-EMF amplitude at rated speed, calculated by (19). C_f is the penalty function when the constraints functions $g_1(x)$ and $g_2(x)$ are not satisfied with the limitations $C_f = 100$, otherwise $C_f = 1$. Table III shows the parameters used in the AMOBH algorithm in this study.

TABLEIII

AMOBH ALGORITHM PARAMETERS

PARAMETERS	Sym.	Value
Dimension of vector	D	5
Number of objectives	n_{objs}	3
Max iterations	T	200
Star size	N_s	100
Maximum elite learning-rate	$Els\text{-}max$	0.4
Minimum elite learning-rate	$Els\text{-}min$	0.1

Although the thrust and the magnetic fields have nothing to do with variable *N* (number of coils), it is necessary to establish the variable *N* (actually *Nr* or *Nz*) to calculate the winding resistance for copper loss calculation. Also, the variable *N* is significant to calculate the back-EMF precisely. To take full advantage of the power driver's capacity, the amplitude of one phase back-EMF is limited within a range from 200 V to 350V. Another constraint is that the thrust must be more than 250 N to ensure the impact energy.

To speed up the optimization process, the variable N is not a random value but is pre-estimated as (27) after the other variables are assigned.

$$N_{max} = \frac{E_{mmax}}{8\pi\tau f B_{av} R_{av}},\ N_{min} = \frac{E_{mmin}}{8\pi\tau f B_{av} R_{av}} \qquad (27)$$

where $B_{av} = \dfrac{\int_{R_{i1}}^{R_s} B_{rm}(r_i)\,dr_i}{R_s - R_{i1}}$ and $R_{av} = R_{i1} + (R_s - R_{i1})/2$.

The Pareto optimal solutions by AMOBH algorithm after T = 200 iterations are shown as Figs. 11–12. Compared to SOPs algorithm, the Pareto optimal solutions by AMOBH here provide more feasible and diverse choices for optimal design. TABLE IV lists three selected optimal solutions corresponding to three objectives domain respectively: the minimum PM volume (optimal design I, region 1 as Fig. 11), the maximum thrust (design II, region 2 as Fig. 11) and the minimum copper loss (design III, region 3 as Fig. 11). Here the sectional area of coil d_i is calculated by (20) and the rated current I_{1N} is the product of d_i and J_m. The actual hammer is made up by three unit motors in parallel. Therefore, the rated current, total thrust, and copper loss are all the sum of three parallel units. Region 3 is the solution area of minimizing copper loss ratio (minimum value 2.09%) in which the PM consumption is the highest (3.1×10^5 mm^3) and the thrust is the lowest (250 N). Region 2 is the solution area of maximizing the thrust (490 N), and region 1 is the solution area of minimizing the PM consumption (0.5×10^5 mm^3) in which the thrust is nearly the lowest (250 N) and the copper loss is the largest (8.97%). Fig. 13 illustrates the Shannon Entropy during the iterations, and it can be seen that the entropy enters approximate convergence after 200 iterations evolutionary calculation. The listed three optimal designs also show that different optimization goals conflict with each other.

What is more, the global optimal solutions (Pareto solutions) set as shown in Fig. 11 and Fig. 12 can help to choose the best one for the actual application-oriented design requirements. Unlike the SOPs, the final selection can take advantages of the comparisons among actual physical quantities such as thrust, back-EMF, copper loss, and PM volume directly. In this application of the electromagnetic hammer we can firstly find the best ones corresponding to thrust objective (e.g. F > 400N), then to consider the copper loss performance, the Pareto optimal solutions set is downsized furtherly. If there are no ideal solutions to meet the copper loss conditions, the first step can be modified and then continue. The third step is to choose the final one according to the cost objective (less PM volume). Here design II is selected for the final Pareto optimal solution. Compared to the initial design, the thrust performance is enhanced by 34% and copper loss is reduced by 18.55% while the PM volume increases approximately by 95%.

TABLE IV COMPARISON AMONG THREE OPTIMAL DESIGNS

Variables and Performance	Symbol	Initial Design	Optimal Design I	Optimal Design II*	Optimal Design III
Outer radius of coil (mm)	R_s	34	33.8	**34**	34
Outer radius of PM (mm)	R_m	17	14.6	**20.5**	26.1
Inner radius of PM (mm)	R_{i2}	9	9.4	**8.1**	8.2
Radial height of PM (mm)	W_2	8	4.2	**12.4**	17.9
Radial height of coils (mm)	W_1	16	19.2	**12.5**	6.9
Width of PM (mm)	$2b$	60	70	**68.8**	68.3
Number of coils	N	350	726	**286**	203
Number of radial coils	Nr	14	22	**11**	7
Number of axial coils	Nz	25	33	**26**	29
Sectional area of coil (mm^2)	di	1.09	0.63	**0.77**	0.81
Thrust (N)	F	318	310	**427**	345
Rated current of one phase (A)	I_{1N}	4.36	2.53	**3.07**	3.26
Rated current of three phases (A)	I_N	13.08	7.59	**9.21**	9.78
Copper loss (W)	P_{cua}	168	180	**137**	82.9
Copper loss ratio (%)	η	5.44%	6.8%	**3.44%**	2.59%
Peak phase back-EMF (V)	E_m	208	352	**330**	359
PM Volume (mm^3)	V	78414	54889	**153304**	263480

The performance comparisons among the AMOBH and two popular MOEAs (in the same conditions): MOEA/D and MOPSO [24] are carried out as Fig. 14 and Fig. 15. The consumption time of AMOBH is about 2604 seconds, that of MOPSO is about 3108 seconds, and that of MOEA/D is about 1837 seconds. Although MOEA/D is the fastest, the diversity of its Pareto solutions set is the worst against the other two algorithms. In terms of population diversity, AMOBH outperforms MOEA/D. In general, the comprehensive performance of AMOBH is the best. The whole solution time is greatly shortened which is nearly the same time as one TS-2D FEA.

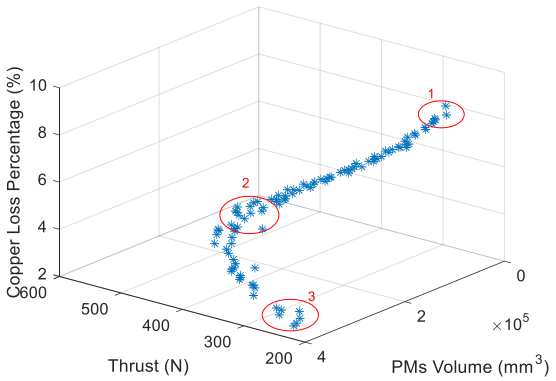

Fig. 11. The optimization results by AMOBH algorithm at T = 200 (View 1)

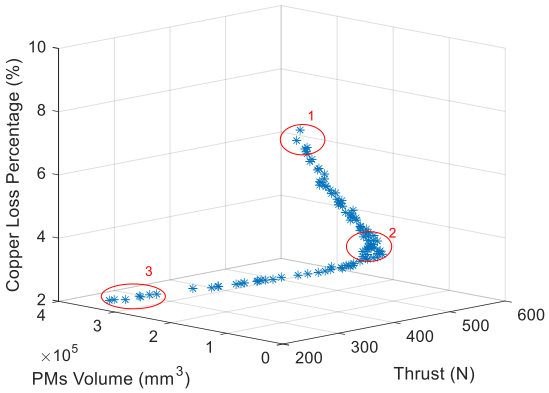

Fig. 12. The optimization results by AMOBH algorithm at T = 200 (View 2)

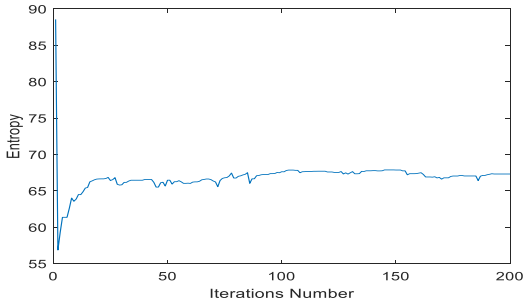

Fig. 13. The Shannon Entropy during T = 200 Iterations Evolution

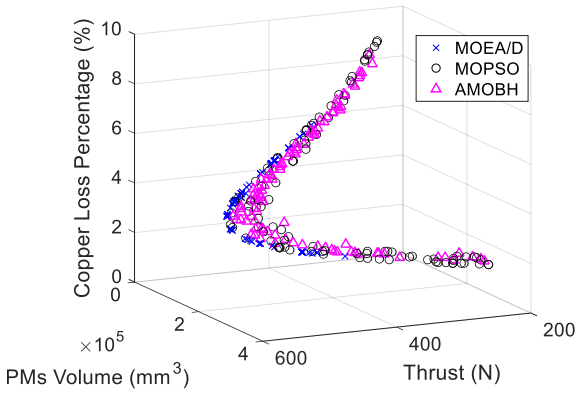

Fig. 14. The comparison among three MOEAs (View 1)

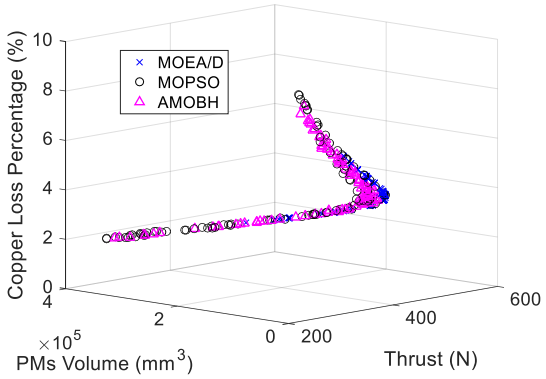

Fig. 15. The comparison among three MOEAs (View 2)

V. FEA AND EXPERIMENTAL VERIFICATION

To validate the analysis presented in the paper, a prototype LPMSM of optimal Pareto design II listed in Table IV has been manufactured and tested for the comparison with the analytical and FE results.

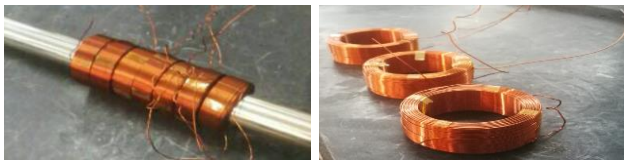

Fig. 16. The pancake windings of the tubular LPMSM before assembling

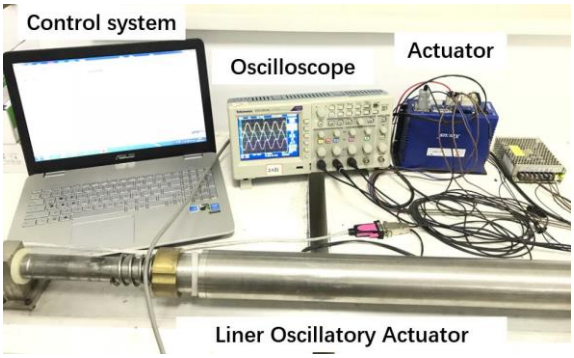

Fig. 17. Physical diagram of the test platform

Fig. 16 is the diagram of pancake windings of the LPMSM before they were assembled into the shell. Fig. 17 is the prototype and the thrust and back-EMF test platform. The thrust comparisons between the AM and TS-2D FE are as Fig. 18. It can be seen that the thrust calculated by analytical method is slightly larger than that of 2D FE model. The two thrust ripple waveforms are very close. Fig. 19 is the thrust comparisons among the analytical method, TS-2D FE and the experiments under different phase current. The thrust error between the analytical method and experiment is less than 9%.

The three-phase back-EMF waves by 2D FEA and the actual measured phase back-EMF of the prototype are as Fig. 20, showing that the phase peak value of the 2D FEA is 325 V and that by experiment at 3.6 m/s is 322 V. Correspondingly the phase peak value calculated by analytical method is 330 V, which is also slightly larger. The discrepancies in thrust and back-EMF result from the factor that the radial flux density calculated by the simplified one-layer AM is larger than that by 2D FEA, although the flat waveforms of two methods are nearly the same, the rising edge of the waveform in one-layer AM is not so precipitous, and it does not take the iron core between the PM into account. In general, the comparison shows that the errors are quite small which can be accepted, especially in electrical MOEAs solution.

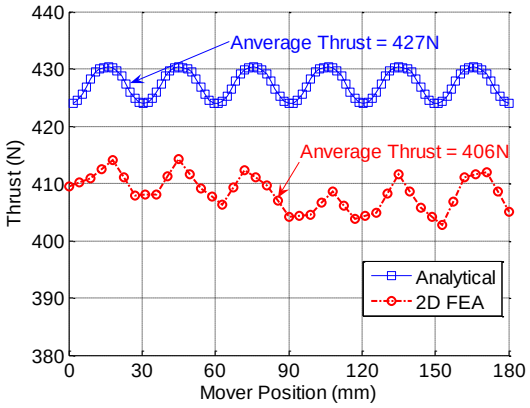

Fig. 18. Thrust curves by analytical method and TS-2D FEA

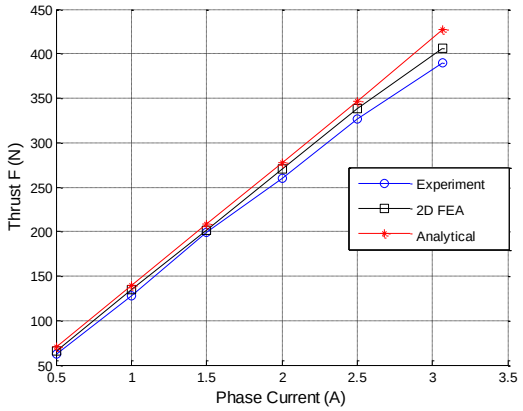

Fig. 19. Thrust comparison among analytical, 2D-FEA and the experiment

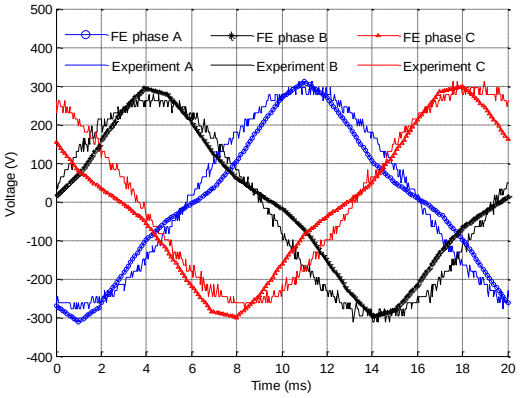

Fig. 20. Back-EMF curve of 2D finite element model and measured back-EMF curves.

VI. Conclusion

This paper presented a multi-objective design optimization of tubular coreless LPMSM based on AMOBH algorithm. A simplified and accurate one-layer AM of the tubular coreless LPMSM was

presented, which can significantly reduce the computation time compared with the multi-layer models. At the same time, the accuracy is relatively high and the thrust errors of the FEA and experiments are less than 10%. The MOEAs can provide more diversified and global optimization results for the multi-objective optimization design of the tubular coreless LPMSM. They are efficient and simple in implementation, and can be extended to the multi-objective optimization of other electrical machines.

REFERENCES

[1] Z. Z. Liu, F. L. Luo, and M. H. Rashid, "Robust high speed and high precision linear motor direct-drive XY-table motion system," *IEE Proc.: Control Theory Appl.*, vol. 151, no. 2, pp. 166-173, 2004.

[2] P. D. Pfister and Y. Perriard, "Very-high-speed slotless permanent-magnet motors: analytical modeling, optimization, design, and torque measurement methods," *IEEE Trans. Ind. Electron.*, vol. 57, no. 1, pp. 296-303, 2010.

[3] J. R. Gomez, R. F. Garcia, J. C. Carril, and M. R. Gómez, "A review of room temperature linear reciprocating magnetic refrigerators," *Renewable Sustainable Energy Rev.*, vol. 21, no. 5, pp. 1-12, 2013.

[4] I. Boldea, "Linear electromagnetic actuators and their control: A review," *EPE J.*, vol. 14, no. 1, pp. 43-50, 2004.

[5] L. H. Zheng, J. X. Jin, Y. G. Guo, W. Xu, and J. G. Zhu, "Performance analysis of an HTS magnetic suspension and propulsion system with a double-sided HTS linear synchronous motor," *IEEE Trans. Magn.*, vol. 48, no. 2, pp. 655-658, 2012.

[6] J. Wang, D. Howe, and G. W. Jewell, "Fringing in tubular permanent-magnet machines: Part I. magnetic field distribution, flux linkage, and thrust force," *IEEE Trans. Magn.*, vol. 39, no. 6, pp. 3507-3516, 2003.

[7] A. Souissi, M. W. Zouaghi, and I. Abdennadher, *et al*., "MEC-based modeling and sizing of a tubular linear PM synchronous machine," *IEEE Trans. Ind. Appl.*, vol. 51, no. 3, pp. 2181-2194, 2015.

[8] T. Wu, Y. Tang, S. Tang, *et al*., "Design and analysis of a new down-the-hole electromagnetic hammer driven by tube linear motor," *IET Elect. Power Appl.*, vol. 11, no. 9, pp. 1558-1565, 2017.

[9] T. Wu, K. Lu, J. G. Zhu, *et al*., "Calculation of eddy current loss in a tubular oscillatory LPMSM using computationally efficient FEA," *IEEE Trans. Ind. Electron.*, DOI: 10.1109/TIE.2018.2874586, 2018.

[10] G. Lei, C. C. Liu, J. G. Zhu, and Y. G. Guo, "Techniques for multilevel design optimization of permanent magnet motors," *IEEE Trans. Energy Convers.*, vol. 30, no. 4, pp. 1574-1584, 2015.

[11] Z. Xiang, X. Zhu, L. Quan, *et al.*, "Multilevel design optimization and operation of a brushless double mechanical port flux-switching permanent-magnet motor," *IEEE Trans. Ind. Electron.*, vol. 63, no. 10, pp. 6042-6054, 2016.

[12] Y. Wang, S. Niu, and W. Fu, "Sensitivity analysis and optimal design of a dual mechanical port bidirectional flux-modulated machine," *IEEE Trans. Ind. Electron.*, vol. 65, no. 1, pp. 211-220. 2018.

[13] S. Vaez-Zadeh and A. H. Isfahani, "Multi-objective design optimization of air-core linear permanent-magnet synchronous motors for improved thrust and low magnet consumption," *IEEE Trans. Magn.*, vol. 42, no. 3, pp. 446-452, 2006.

[14] S. G. Min and B. Sarlioglu, "3-D performance analysis and multi-objective optimization of coreless-type PM linear synchronous motors," *IEEE Trans. Ind. Electron.*, vol. 65, no. 2, pp. 1855-1864, 2018.

[15] G. Lei, C. C. Liu, J. G. Zhu, and Y. G. Guo, "Multilevel robust design optimization of a superconducting magnetic energy storage based on a benchmark study," *IEEE Trans. Appl. Supercond.*, vol. 26, no. 7, 2016.

[16] J. Wang and D. Howe, "Tubular modular permanent-magnet machines equipped with quasi-Halbach magnetized magnets-part I: magnetic field distribution, EMF, and thrust force," *IEEE Trans. Magn.*, vol. 41, no. 9, pp. 2470-2478, 2005.

[17]J. Wang and D. Howe, "Tubular modular permanent-magnet machines equipped with quasi-Halbach magnetized magnets-part II: armature reaction and design optimization," *IEEE Trans. Magn.*, vol. 41, no. 9, pp. 2479-2489, 2005.

[18]P. He, Z. Jiao Z, L. Yan, *et al.*, "Thermal optimization of a tubular linear oscillating motor for directly driven LEHA application," *Numer. Heat Transf. A-Appl.*, vol. 69, no. 4, pp. 383-400, 2016.

[19]J. G. Zhu, S. Y. R. Hui, and V. S. Ramsden, "A generalized dynamic circuit model of magnetic cores for low-and high-frequency applications. I. Theoretical calculation of the equivalent core loss resistance," *IEEE Trans. Power Electron.*, vol. 11, no. 2, pp. 246-250, 1996.

[20]P. Zhang, G. Y. Sizov, J. He, *et al.*, "Calculation of magnet losses in concentrated-winding permanent-magnet synchronous machines using a computationally efficient finite-element method," *IEEE Trans. Ind. Appl.*, vol. 49, no. 6, pp. 2524-2532, 2013.

[21]G. Lei, J. Zhu, Y. Guo, C. Liu, and B. Ma, "A review of design optimization methods for electrical machines," *Energies*, vol. 10, article 1962, 2017.

[22]E. Zitzler, K. Deb, and L. Thiele, "Comparison of multi-objective evolutionary algorithms: empirical results," *Evol. Comput.*, vol. 8, no. 2, pp. 173-195, 2000.

[23]R. Cheng, Y. Jin, M. Olhofer, *et al.*, "A reference vector guided evolutionary algorithm for many-objective optimization," *IEEE Trans. Evolutionary Computation*, vol. 20, no. 5, pp. 773-791, 2016.

[24]C. A. C. Coello, G. T. Pulido and M. S. Lechuga, "Handling multiple objectives with particle swarm optimization," *IEEE Trans. Evol. Comput.*, vol. 8, no. 3, pp. 256-279, 2004.

[25]K. Deb, A. Pratap, S. Agarwal, *et al.*, "A fast and elitist multi-objective genetic algorithm: NSGA-II," *IEEE Trans. Evol. Comput.*, vol. 6, no. 2, pp. 182-197, 2002.

[26]Q. Zhang and H. Li, "MOEA/D: A Multiobjective Evolutionary Algorithm Based on Decomposition," IEEE *Trans. Evol. Comput.*, vol. 11, no. 6, pp. 712-731, 2007.

[27]C. Wu, T. Wu, K. Y. Fu, *et al.*, "AMOBH: adaptive multi-objective black hole algorithm," *Comput. Intell. Neurosci.*, vol. 9, article 6153951, 2017.

[28]Zhang, Junqi, *et al*. "Random black hole particle swarm optimization and its application," *Neural Networks and Signal Processing, 2008 International Conference on IEEE*, 2008.

[29]S. H. Wang and G. Y. Xiong, "Analysis of air-gap field in a new tubular linear PM motor with moving coil," *Trans. China Electrotech. Society*, vol. 22, no. 5, pp. 40-44, 2007.

[30]J. H. Zhao, X. F. Zhang, J. H. Zhang, *et al.*, "Field and thrust analysis of tubular permanent magnet linear synchronous motor," *Electr. Mach. Control*, no. 1, pp. 12-17, 2010.

[31]W. Hu, G. G. Yen, and X. Zhang, "Multi-objective Particle Swarm Optimization Based on Pareto Entropy," *J. Softw.*, vol. 2014, no. 5, pp. 1025-1050, 2014.

Tao Wu (M'19) received the B.E. degree and the M.S. degree from the China University of Geoscience, Hubei, China, in 2001 and 2004, respectively; and the Ph.D. degree in motors and electrical appliances from the Huazhong University of Science and Technology, Wuhan, China, in 2010.

He is currently an associate professor with the School of Automation, China University of Geoscience. His current research interests include motors and controls, design and optimization of electrical systems, and equipment and instruments.

Zhenan Feng received the B.E. degree in automation in 2018 from the School of Automation, China University of Geosciences, Hubei, China, where she is currently working toward the master's degree in control science and engineering.

Her current research interests include motors and controls, and design and optimization of electrical systems.

Chong Wu was born in Zhejiang Province, China. He received the B.E. degree from the School of Automation, China University of Geosciences, Wuhan, China, in

2018. Since then, he is working toward the Ph.D. degree in electronic engineering from the Department of Electronic Engineering, City University of Hong Kong, Hong Kong.

His current research interests include multi-objective optimization, graph theory, evolutionary computation, image processing, and pattern recognition.

Gang Lei (M'14) received the B.S. degree in mathematics from Huanggang Normal University, Huanggang, China, in 2003, and the M.S. degree in mathematics and the Ph.D. degree in electrical engineering from the Huazhong University of Science and Technology, Wuhan, China, in 2006 and 2009, respectively.

He is currently a Senior Lecturer with the University of Technology Sydney, Sydney, Australia. His research interests include design optimization and control of electrical drive systems and renewable energy systems.

Youguang Guo (S'02–M'05–SM'06) received the B.E. degree from the Huazhong University of Science and Technology, Wuhan, China, in 1985, the M.E. degree from Zhejiang University, Hangzhou, China, in 1988, and the Ph.D. degree from the University of Technology Sydney (UTS), Sydney, Australia, in 2004, all in electrical engineering.

He is currently an Associate Professor with the UTS. His research interests include measurement and modeling of properties of magnetic materials, numerical analysis of electromagnetic field, electrical machine design optimization, and power electronic drives and control.

Jianguo Zhu (S'93–M'96–SM'03) received the B.E. degree from the Jiangsu Institute of Technology, Zhenjiang, China, in 1982, the M.E. degree from the Shanghai University of Technology, Shanghai, China, in 1987, and the Ph.D.

degree from the University of Technology Sydney (UTS), Sydney, Australia, in 1995, all in electrical engineering.

He is currently a Professor and Head of School for the School of Electrical and Information Engineering, University of Sydney, Australia. His current research interests include electromagnetics, magnetic properties of materials, electrical machines and drives, power electronics, and green energy systems.

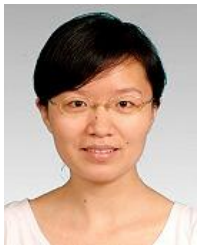

Xinmei Wang received the B.S. degree and the M.S. degree in computer science and technology from the Wuhan University of Technology, Hubei, China, in 2003 and 2006, respectively; and the Ph.D. degree in control theory and engineering from the South China University of Technology, Guangdong, China, in 2009.

She is currently a lecturer with the School of Automation, China University of Geoscience. Her current research interests include stability analysis and control of time delay system, and visual servo and its control system with time delay compensation and optimization.